Lawrence Berkeley National Laboratory
LBL Publications

Title

Hole-Carrier-Dominant Transport in 2D Single-Crystal Copper

Permalink
https://escholarship.org/uc/item/6bn7s3rr

Journal
Advanced Materials, 36(36)

ISSN
0935-9648

Authors
Ok, Jong Mok
Kang, Kyungrok
Hyun, Jounghoon
et al.

Publication Date
2024-09-01

DOI
10.1002/adma.202403783

Copyright Information
This work is made available under the terms of a Creative Commons Attribution-NonCommercial License, available at https://creativecommons.org/licenses/by-nc/4.0/

Peer reviewed

eScholarship.org Powered by the California Digital Library
University of California

Check for updates

ADVANCED MATERIALS
www.advmat.de

Hole-Carrier-Dominant Transport in 2D Single-Crystal Copper

Jong Mok Ok, Kyungrok Kang, Jounghoon Hyun, Chan-Young Lim, Seonggeon Gim, Jinwoong Hwang, Jonathan D. Denlinger, Miyeon Cheon, Binod Regmi, Ji-Eun Lee, Hyejin Ryu, Su Jae Kim, Yousil Lee, Young-Hoon Kim, Young-Min Kim, Yeongkwan Kim, Seong-Gon Kim,* Heejun Yang,* and Se-Young Jeong**

In 2D noble metals like copper, the carrier scattering at grain boundaries has obscured the intrinsic nature of electronic transport. However, it is demonstrated that the intrinsic nature of transport by hole carriers in 2D copper can be revealed by growing thin films without grain boundaries. As even a slight deviation from the twin boundary is perceived as grain boundaries by electrons, it is only through the thorough elimination of grain boundaries that the hidden hole-like attribute of 2D single-crystal copper can be unmasked. Two types of Fermi surfaces, a large hexagonal Fermi surface centered at the zone center and the triangular Fermi surface around the zone corner, tightly matching to the calculated Fermi surface topology, confirmed by angle-resolved photoemission spectroscopy (ARPES) measurements and vivid nonlinear Hall effects of the 2D single-crystal copper account for the presence of hole carriers experimentally. This breakthrough suggests the potential to manipulate the majority carrier polarity in metals by means of grain boundary engineering in a 2D geometry.

1. Introduction

Solid-state electronics, including transistors, diodes, and various sensors, use the flow and control of conduction electrons in semiconducting channels and metal electrodes. Among the various characteristics of materials, the electronic band structure near the Fermi surface (FS) determines the behavior of conduction electrons, which is a key feature to be exploited for device applications and design. Thus, the polarity, density, and mobility of charge carriers have been manipulated and optimized for semiconductors. However, the effective design of electronic properties has not been applied for other critical electronic components with noble metals, such as copper (Cu), which restricts the full potential of materials for conceptually new devices.

J. M. Ok
Department of Physics
Pusan National University
Busan 46241, Republic of Korea

K. Kang, Y.-H. Kim, Y.-M. Kim
Department of Energy Science
Sungkyunkwan University (SKKU)
Suwon 16419, Republic of Korea

J. Hyun, C.-Y. Lim, S. Gim, Y. Kim, H. Yang, S.-Y. Jeong
Department of Physics
Korea Advanced Institute of Science and Technology (KAIST)
Daejeon 34141, Republic of Korea
E-mail: yeongkwan@kaist.ac.kr; h.yang@kaist.ac.kr; sjeong9@mgh.harvard.edu

The ORCID identification number(s) for the author(s) of this article can be found under https://doi.org/10.1002/adma.202403783

© 2024 The Author(s). Advanced Materials published by Wiley-VCH GmbH. This is an open access article under the terms of the Creative Commons Attribution-NonCommercial License, which permits use, distribution and reproduction in any medium, provided the original work is properly cited and is not used for commercial purposes.

DOI: 10.1002/adma.202403783

J. Hwang
Department of Physics and Institute of Quantum Convergence Technology
Kangwon National University
Gangwon 24341, Republic of Korea

J. Hwang, J. D. Denlinger, J.-E. Lee
Advanced Light Source
Lawrence Berkeley National Laboratory
Berkeley, CA 94720, USA

M. Cheon, S. J. Kim
Crystal Bank Research Institute
Pusan National University
Busan 46241, Republic of Korea

B. Regmi, S.-G. Kim
Department of Physics and Astronomy
Mississippi State University
Mississippi State, MS 39762, USA
E-mail: sk162@msstate.edu

J.-E. Lee, H. Ryu
Center for Spintronics
Korea Institute of Science and Technology (KIST)
Seoul 02792, Republic of Korea

Y. Lee
Copper Innovative Technology (CIT) Co.
Busan 46285, Republic of Korea

The Fermi surface of metals is overwhelmed by random scattering at numerous defects such as grain boundaries (GBs) during transport.[1] GBs are formed with a density more than ≈10^2 μm^{-2} (10^{10} cm^{-2}) in the growth process of metal thin film and are difficult to avoid. The transport of electrons and phonons has been reported to be critically affected by GBs, particularly when the mean free paths (MFPs) of the transport media are longer than the distance between GBs.[2] Additionally, due to the miniaturization of modern electronics, electronic devices are becoming increasingly smaller in size, and there is now a growing demand for 2D electronic materials, including metals. Thus, the synthesis of single-crystalline metals in a 2D geometry is an interesting issue; nucleation in the initial growth stage generates innumerable, separated grains.[3] While there have been tremendous efforts to minimize the GBs in 2D metals, complete suppression of GBs has not been achieved to date, particularly for large-scale noble metals (e.g., Cu and Au) with thicknesses down to 10 nm.[3–6] The GBs generated in the initial growth state cause scattering of electrons and consequently lose their intrinsic properties. For example, the resistivity of noble metals increases as their thickness decreases, which remarkably appears in their 2D limit.[7–9] Despite the large interest in 2D materials sparked by the discovery of graphene, the 2D properties of novel metal have still not been well explored. Thus, thickness control has been conducted for engineering issues such as realizing a high conductivity with the least amount of metal for device fabrication. The main physical origin for the resistivity change with thickness is the modified conduction mechanism in the metal along with its GB features, as explained in the mesoscopic transport regime. In the absence of GBs and with a thickness below the MFP of transport media, unconventional transport in metals could be conceived.[9–11]

In this study, we demonstrate counterintuitive hole-carrier-dominant (HCD) transport in ultraclean 2D Cu induced by a combination of the 2D geometry of single-crystal Cu thin film (SCCF) and GB-free growth. The GB density could be strongly suppressed in 2D Cu fabricated by an atomic sputtering epitaxy (ASE) system.[12,13] In the absence of GBs, another category of geometrical features, twin boundaries (TBs), could be investigated, which reveals their distinct roles in transport compared with GBs. Rigorous characterization of the electronic band structure of our 2D Cu has been conducted via structural analysis, angle-resolved photoemission spectroscopy (ARPES) measurements, and Hall measurement with two-carrier model fitting analysis. In contrast to the electron carriers in conventional Cu, suppression of GBs in 2D SCCF reveals HCD transport. The first-principles calculations theoretically and the ARPES measurements experimentally explain the HCD transport by the concave geometry of the Fermi surface in the 2D Cu with zero GBs. The distinct nature of the transport suggests a breakthrough in manipulating the apparent polarity of charge carriers in metals[14–17] based on GB engineering in a 2D geometry.

S.-Y. Jeong
Gordon Center for Medical Imaging
Department of Radiology
Massachusetts General Hospital and Harvard Medical School
Boston, MA 02114, USA
S.-Y. Jeong
Department of Optics and Mechatronics Engineering
Engineering Research Center for Color-Modulated Extra-Sensory Perception Technology
Pusan National University
Busan 46241, Republic of Korea

2. Results and Discussion

2.1. Fermi Surface Reconstruction of 2D Cu(111)

To understand the intrinsic properties of 2D Cu thin films, we calculated the electronic band structure of Cu in the 2D limit using a 42 monolayer (ML) Cu(111) thin film whose thickness is less than 10 nm. If Cu reaches the 2D limit by reducing the thickness along any spatial coordinate down to the nanometric scale, then the quantum confinement leads to a reconstruction of the ordinary 3D Fermi surface (**Figure 1**a) and consequently generates a 2D Fermi surface composed of a series of 2D subbands (Figure 1b). In the case of thinning down Cu along the (111)-direction, an unusual modification of the 2D Fermi surface forming concave-shaped Fermi surface near *K*-point due to the necks along (111)-direction in the 3D Fermi surface is predicted (Figure 1b). Fermi surfaces in the middle (inner rings) are the electron orbits (scaled by $\frac{eH}{\hbar c}$) with higher potential energy and lower Fermi velocity than that of the outermost surface, carriers in these orbits are electrons. We note that the outermost concave-shaped Fermi surface has a negative curvature, resulting in the development of hole carriers.[18] This is because the conduction carriers moving along the convex- and concave-shaped Fermi surfaces will contribute to different polarity based on the geometrical interpretation of Fermi surface,[18] as previously observed in quasi-2D systems such as $YBa_2Cu_3O_{7-x}$, $La_{2-x}Sr_xCuO_4$, FeSe, and $Ba(Fe_{1-x}Co_x)_2As_2$.[19–23] It becomes rather clear in the periodic zone scheme that 2D FSs are composed with electron pocket at the zone center (denoted with blue circles) and the hole pockets at the zone corner (red circles) as displayed in Figure 1c.

In order to experimentally confirm the expected reconstruction of the Fermi surface, ARPES was employed to directly measure the electronic structure on the (111) plane of 80 nm thick SCCF. In sharp contrast to the Fermi surface topology of 3D bulk Cu (Figure 1a), the observed Fermi surface taken at the k_z = 0 plane (Figure 1d) and its curvature plot (Figure 1e) shows sixfold symmetric Fermi surface with two types of FSs, a large hexagonal FS centered at the zone center and the triangular FS around the zone corner, tightly matching to the calculated FS topology (Figure 1b,c). Further, detailed band dispersion given in Figure 1f,g exhibits two types of bands clearly; the electron (hole) with $\frac{\partial^2 E}{\partial k^2} > 0$ ($\frac{\partial^2 E}{\partial k^2} < 0$), which forms hexagonal (triangular) FSs, respectively, confirming the carrier type of each FS and thus the existence of hole carrier. We note that such FS topology consistently appears in SCCFs of 40 and 20 nm thicknesses (Figure S1, Supporting Information). The theoretically calculated side view of the Fermi surface of 42 ML Cu(111) thin film and the effective band structure of 42 ML Cu(111) thin film along the special *k*-points obtained are also given in Figure S1 (Supporting Information). The hole band extracted from band structure calculations was compared with the ARPES measurements in Figure S2 (Supporting Information).

© 2024 The Author(s). Advanced Materials published by Wiley-VCH GmbH

15214095, 2024, 36, Downloaded from https://onlinelibrary.wiley.com/doi/10.1002/adma.202403783, Wiley Online Library on [12/09/2024]. See the Terms and Conditions (https://onlinelibrary.wiley.com/terms-and-conditions) on Wiley Online Library for rules of use; OA articles are governed by the applicable Creative Commons License

15214095, 2024, 36, Downloaded from https://onlinelibrary.wiley.com/doi/10.1002/adma.202403783, Wiley Online Library on [12/09/2024]. See the Terms and Conditions (https://onlinelibrary.wiley.com/terms-and-conditions) on Wiley Online Library for rules of use; OA articles are governed by the applicable Creative Commons License

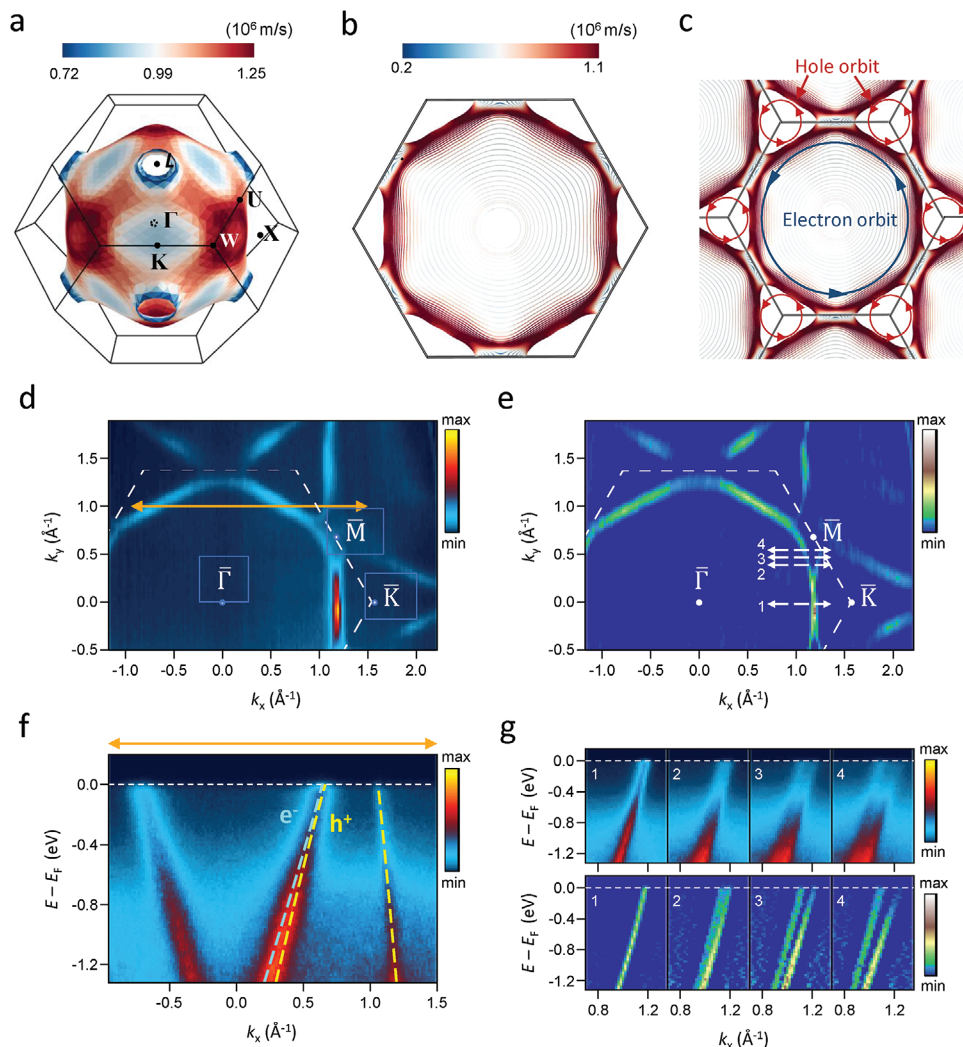

Figure 1. Fermi surfaces of 2D copper. a) Calculated Fermi surfaces of Cu in the 3D limit. Color indicates the magnitude of the Fermi velocity. b) Calculated Fermi surfaces of Cu(111) thin film in the 2D limit. The inner surfaces of 2D limit Fermi surface are the result of quantum confinement along the out-of-plane direction. c) Calculated Fermi surfaces of 2D Cu in periodic zone scheme. Blue (red) circle represents the electronic (hole) orbit. d) Fermi surface map of 80 nm thick Cu(111) film obtained by ARPES measurement. White dashed line and dot indicate surface Brillouin zone (BZ) and high-symmetry points, respectively. e) Curvature plot of (d), showing separately existing hexagonal and triangular FSs. f) Band dispersion along the orange arrow line indicated in panel (d). Cyan and yellow dashed lines are guides to the eye for the electron and hole band, respectively. g) Band dispersions (upper) and its curvature plots (lower) along the dashed lines in **e**, demonstrating two clearly resolved electron and hole band.

Here, our observation not only demonstrates the existence of hole carrier but also elucidates the unique characteristics of our system. Previously, sixfold symmetric Fermi surface without the "L gap necks" of bulk state was reported in Cu(111) films only with few-monolayer thicknesses. However, thickness of our system is much larger than that, rather close to bulk system. The photon-energy-dependent measurement, which examines the dimensionality of the electronic structure, returns mixed nature of electronic structure; the expected 2D nature of sixfold symmetric FS is captured, together with ordinary 3D electronic structure of bulk system around $k_z = \pi$ point (Figure S3, Supporting Information). This mixed nature clearly indicates that our system belongs to the bulk system but exhibits the behavior of 2D by virtue of unique properties of our SCCF–GB-free, atomically flat, and robust against the oxidization.

2.2. Nonlinear Hall Effects in 2D Copper

Given that we directly examined the HCD transport through Hall measurement, the Fermi surface of Cu originates from the free-electron-like s band, while fully populated d electrons do not contribute to the electronic band near the Fermi level. The s-band character of Cu ensures its high enough conductivity and a Fermi velocity as large as $\approx 1.1 \times 10^6$m s^{-1} which is demonstrated in Figure 1a with the color mapping. 3D Cu has a well-known 3D Fermi surface with necks along the (111)-direction, from which conventional magnetoresistance properties have arisen.[24] The calculated Fermi surface topology of 3D Cu has open necks only along three direction along (111) (**Figure** 2a).[25] The bulk single-crystal Cu thicker than 1 µm (Figure 2b) shows an ordinary Hall effect with a single carrier (electron) density of

 © 2024 The Author(s). Advanced Materials published by Wiley-VCH GmbH

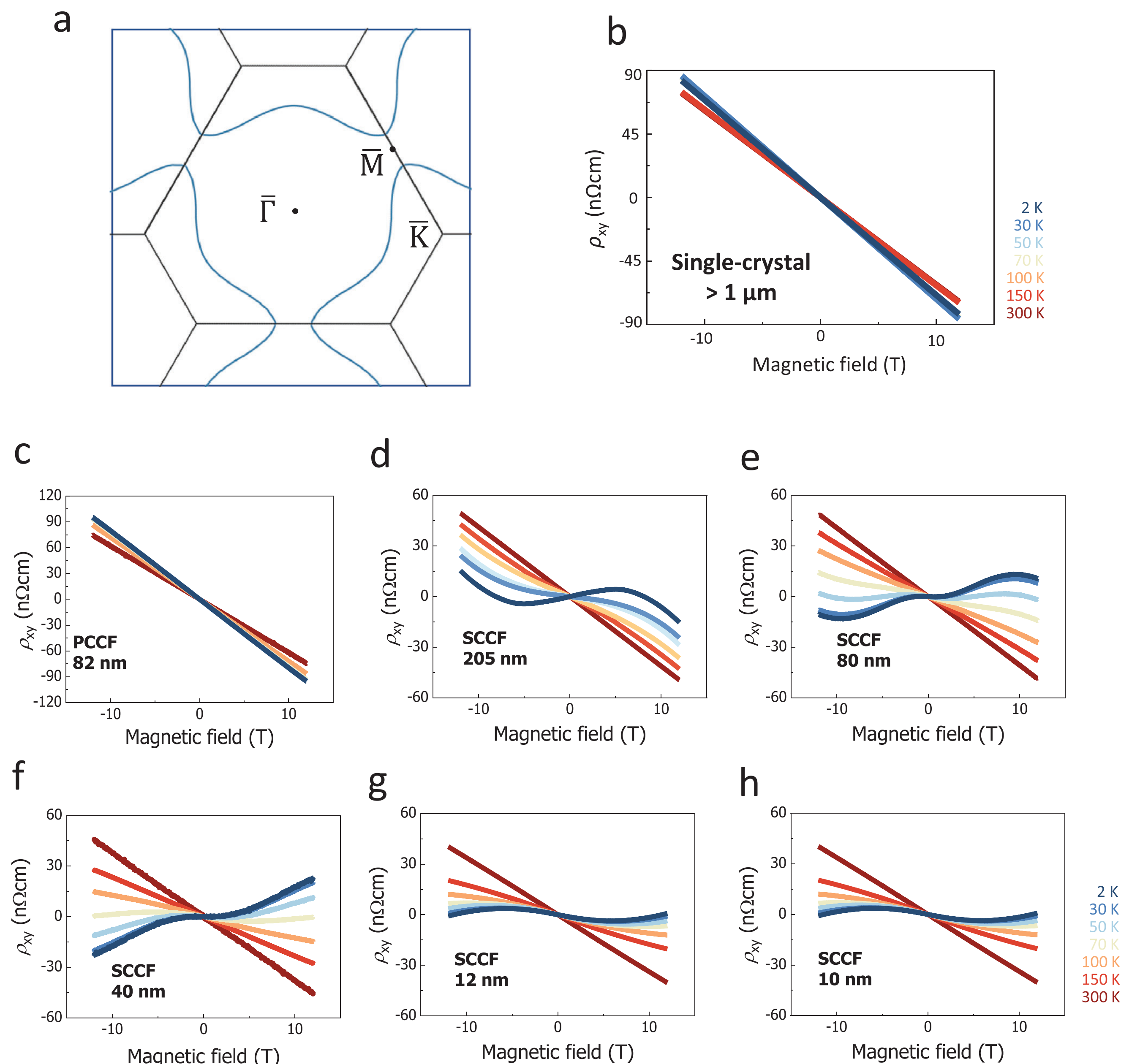

Figure 2. Fermi surfaces and Hall effects in 3D and 2D Cu. a) Calculated Fermi surface contour of Cu in 3D limit with open necks only along three directions of {111}. b) All curves measured for the single-crystal samples thicker than 1 µm are linear and show almost no temperature dependence meaning for carriers definitely to be electrons in 3D regime. c) Hall effect of polycrystalline Cu (PCCF) with a thickness of 82 nm. d–h) measured nonlinear Hall effects of SCCFs with thicknesses of d) 205 nm, e) 80 nm, f) 40 nm, g) 12 nm, and h) 10 nm.

$n = 9.09 \times 10^{22}$ cm^{-3} at $T = 2$ K, which is consistent with both the known bulk electron density,[26] and the value of polycrystalline copper thin film (PCCF) in the 2D limit (Figure 2c). Although 3D copper also has a concave Fermi surface, this region is very narrow and does not lead to a purely hole-like orbit in the periodic zone scheme (Figure 2a). Thus, it is difficult to observe hole carriers in bulk copper. However, SCCF samples show different behavior in 2D regime. As the thickness of the SCCF sample is deceased to less than 205 nm, the ordinary Hall effect, which shows a linear response to the external magnetic field, changes to a nonlinear Hall effects (NHEs) (Figure 2d–h). The NHE here refers to a deviation from linear dependence on external magnetic field, called the ordinary Hall effect. The appearance of nonlinearity at low temperature starts at a thickness of 205 nm (Figure 2d) and becomes more noticeable at thicknesses of 80 and 40 nm (Figure 2e,f), and is slightly suppressed in thin samples of 12 and 10 nm (Figure 2g,h) approaching to the limit of thin film growth. Based on the measurements of mean free paths of films (Figure S4, Supporting Information), we can assume that Cu samples with a thickness of 1 µm remain in the 3D

© 2024 The Author(s). Advanced Materials published by Wiley-VCH GmbH

15214095, 2024, 36, Downloaded from https://onlinelibrary.wiley.com/doi/10.1002/adma.202403783, Wiley Online Library on [12/09/2024]. See the Terms and Conditions (https://onlinelibrary.wiley.com/terms-and-conditions) on Wiley Online Library for rules of use; OA articles are governed by the applicable Creative Commons License

limit, while SCCF samples with thicknesses of 205, 80, 40, 20, and 10 nm can reach the 2D limit at temperatures below 62, 110, 128, 210, and 300 K, respectively.

Although we have not presented all the data in this study, we did observe NHE in all ASE-grown samples without any GBs below a thickness of 200 nm. This was consistent across all samples without exception. We have provided contour plots of the Hall coefficient R_H at different temperatures and magnetic fields for three representative samples (Figure S5, Supporting Information). These findings indicate a significant correlation between the NHE and observed 2D FS. The concave 2D Fermi surface makes effective mass negative and contributes to "hole carrier" in Hall measurements. It is worth noting that while the NHEs could potentially be caused by ferromagnetism, no evidence of magnetic ordering was detected in our samples (Figure S6, Supporting Information). Therefore, the NHE observed in 2D SCCF is distinct from the anomalous Hall effect caused by magnetism or Berry curvature in the momentum space.[27] Instead, the observed NHEs are well explained by the two-carrier model involving electron and hole carriers, which is further elaborated in Figure 4. Additionally, it is important to mention that the 2D Fermi surfaces with both electron and hole FSs were consistently observed in all SCCF samples where NHE was measured (Figure S1, Supporting Information).

2.3. Hall Effect of Cu(111) Depending on the GB Density

To investigate the origin of NHE in 2D Cu, 40 nm thick SCCFs were prepared, which exhibited maximum nonlinearity. Subsequently, the defect densities of the thin films were adjusted by subjecting them to additional thermal processing. The defect densities of the samples were characterized using electron backscattering diffraction (EBSD) mapping. The first column on the left of **Figure 3a–e** shows normal direction (ND) EBSD maps. The leftmost panel of Figure 3a shows the EBSD map for a relatively high-quality polycrystalline Cu film grown on a Si substrate (poly-GB10^3). The submicrometer-sized grains are oriented in random directions. In contrast, the samples of Figure 3b–e were grown by the ASE method. The ASE raw sample grown under the optimized conditions (about 170 °C) actually had very few GBs.[12] However, in order to determine how the NHE varies with the GB density, the initial ASE pristine sample (ASE-GB10^3, Figure 3b) was grown at 100 °C, which is lower than the optimized temperature condition (≈170 °C), and a series of samples were obtained by additional heat treatments at 450 °C (ASE-GB10^2; Figure 3c), 500 °C (ASE-GB10^1; Figure 3d) and 400 °C (ASE-GB_0; Figure 3e). The power notation of 10 in sample names depicts the order of magnitude of the GB density in each sample. For example, ASE-GB_0 means complete absence of GBs, and ASE-GB10^2 means the existence of a few or several GBs per μm^2 (**Table 1**). The misorientation statistics given in the tables are derived from the EBSD maps with the software of TSL OIM analysis v7 for the area of 174.3 μm^2. The EBSD maps of ASE samples (first panels of Figure 3b–e) are completely blue, indicating that the ASE-grown samples have no random crystal orientation other than Cu(111) for the out-of-plane direction. Upon closer examination of the blue EBSD map (Figure 3b–e, first column), a subtle distinction between two colors becomes apparent. This differentiation is attributed to two distinct crystallographic orientations with ABC stacking and ACB stacking, demarcated by twin boundaries. Typically, the distinct orientations contributing to the color variation in SCCF deviate by less than 1°.

The second panels of Figure 3a–e show the rolling direction (RD) mode EBSD maps with the misorientation angle distributions for the samples. Red and blue lines represent TBs and GBs, respectively. A TB is a boundary between two different crystal lattices that are perfectly aligned along the (111) direction out of plane but are rotated by 60° from each other in-plane and satisfy a rotational symmetry operation.[28] In contrast, a GB generally means a boundary between two grains with an arbitrary angle along the in-plane and out-of-plane directions. In this study, for strict distinction of TBs and GBs, we classify the boundaries as GBs if the in-plane misorientation between two neighboring crystal lattices differs slightly from 60°, even though the two different crystal lattices are perfectly aligned along the (111) direction for the out-of-plane orientation or if the incoherent TB (ITB)[28] separating two neighboring crystal lattices incline more than 1° from the out-of-plane direction. The formation of TBs is inevitable in thin film growth,[28] because in the nucleation process, a crystal orientation must choose one of two stacking orders, such as ABC or ACB....[9] However, TBs do not affect the physical properties such as oxidation and surface quality of the film, while the formation of GB seriously affects the quality, oxidation properties, and electrical properties of metal thin films.[1,13,28] The characteristic of the almost invisible TB to electron can be understood in the fact that the 2D Fermi surface (Figure 1b) is invariant to the exact sixfold rotational symmetry operation. The ASE-grown pristine sample (ASE-GB10^3) has a GB density of ≈10^3 nm μm^{-2} and a TB density of ≈10^3 nm μm^{-2}, while sample poly-GB10^3 has a GB density of ≈10^3 nm μm^{-2} and a TB density of ≈10^3 nm μm^{-2}. The GB density varies depending on the temperatures of thermal process but shows no linear relationship. While samples ASE-GB10^2 (Figure 3c) and ASE-GB10^1 (Figure 3d) treated at 450 and 500 °C have GB densities of ≈10^2 and ≈10^1 nm μm^{-2}, respectively, the GBs completely disappear after heat treatment at 400 °C (ASE-GB_0) (Figure 3e). Because GBs appearing in single-crystalline thin films grown by ASE are almost indistinguishable from TBs, GB density of ASE-GB10^3 is greatly different from that of poly-GB10^3. The acute distinction between GB and TB was precisely presented using transmission electron microscopy (TEM) cross-sectional images (Figure S7, Supporting Information).

The results of Hall measurements are given in the third panels of Figure 3a–e in the form of ρ_{xy} as a function of magnetic field. While sample poly-GB10^3 shows a linear behavior with little temperature dependence, single-crystalline samples ASE-GB10^3 (Figure 3b), ASE-GB10^2 (Figure 3c), and ASE-GB10^1 (Figure 3d) show increasing nonlinearity as the GB density decreases. This indicates that polycrystalline Cu films show linear Hall resistivity with single carriers (i.e., electrons) (Figure S8, Supporting Information), as bulk Cu crystals do. Most notably, sample ASE-GB_0 (Figure 3e) without GBs exhibits a distinct nonlinearity, especially at low temperatures. It shows that GBs seriously affect the electric transport. We also tracked the dependence of electron transport on the TB density. The TB density shows no clear influence on electron transport and NHE, which supports that TBs are almost invisible to electrons.[29] Table 1 summarizes the detailed

© 2024 The Author(s). Advanced Materials published by Wiley-VCH GmbH

15214095, 2024, 36, Downloaded from https://onlinelibrary.wiley.com/doi/10.1002/adma.202403783, Wiley Online Library on [12/09/2024]. See the Terms and Conditions (https://onlinelibrary.wiley.com/terms-and-conditions) on Wiley Online Library for rules of use; OA articles are governed by the applicable Creative Commons License

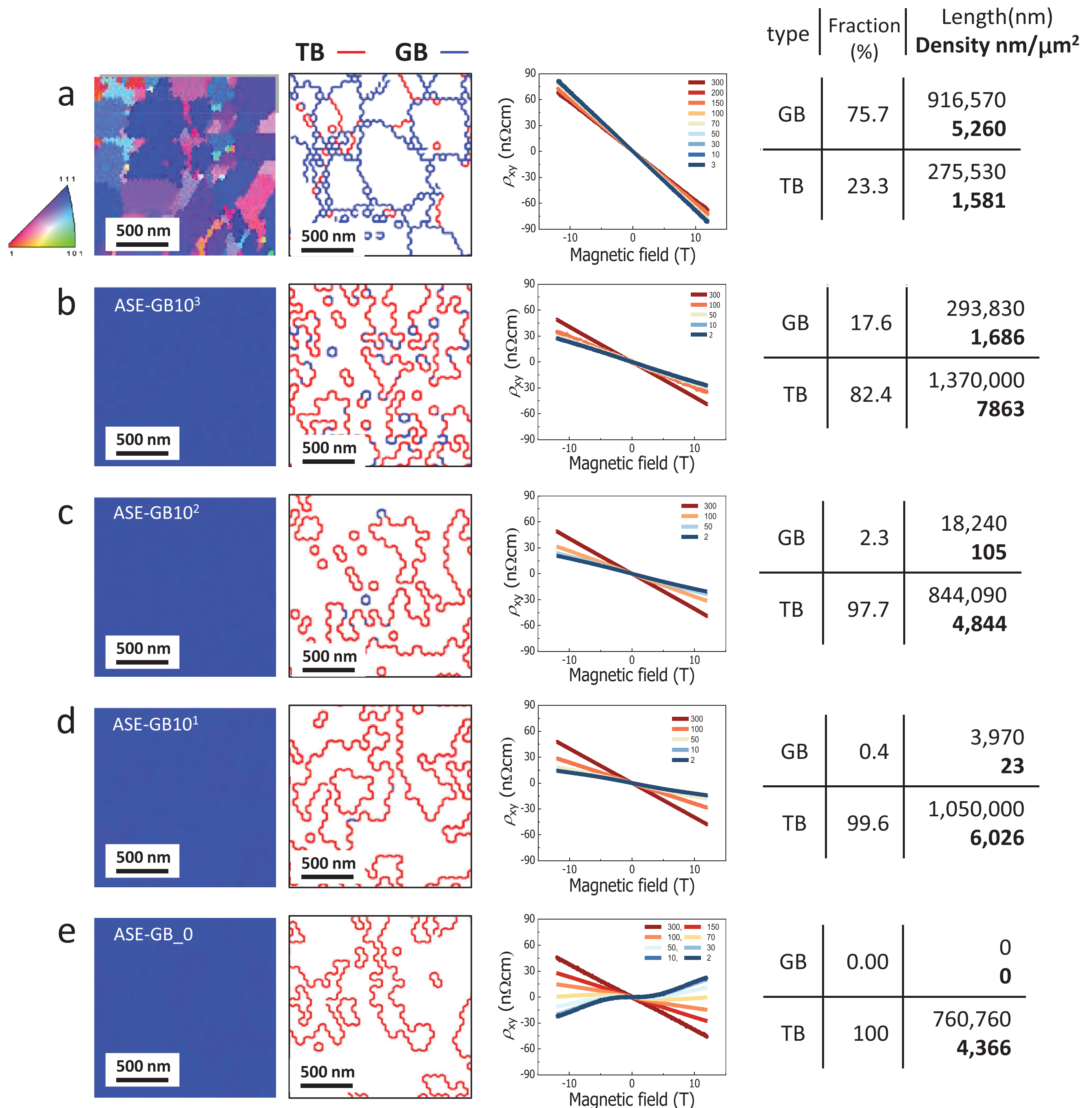

Figure 3. Nonlinear Hall effect depending on the GB densities. a–e) EBSD maps (first column), misorientation angle distributions (second column), NHEs (third column), and fraction of GBs versus TBs (fourth column) of a) a polycrystalline Cu thin film with a GB density of 5260 nm μm^{-2} (poly-GB10^3), b) an ASE-grown pristine single-crystalline Cu thin film with a GB density of 1686 nm μm^{-2} (ASE-GB10^3), and c) heat-treated ASE-grown Cu thin films with different GB densities of 105 nmμm^{-2} (ASE-GB10^2), d) 23 nm μm^{-2} (ASE-GB10^1), and e) 0 nm μm^{-2} (ASE-GB_0). If the two neighboring orientations are rotated more and less than 60° from each other, the misorientations are GBs, marked blue, and if they are rotated by exactly 60° from each other, then the misorientation is TB, marked red.

© 2024 The Author(s). Advanced Materials published by Wiley-VCH GmbH

15214095, 2024, 36, Downloaded from https://onlinelibrary.wiley.com/doi/10.1002/adma.202403783, Wiley Online Library on [12/09/2024]. See the Terms and Conditions (https://onlinelibrary.wiley.com/terms-and-conditions) on Wiley Online Library for rules of use; OA articles are governed by the applicable Creative Commons License

Table 1. GB and TB densities observed in five different samples.

Sample	Boundary type	Fraction [%]	Length [nm]	Density [nm μm^{-2}]
Poly-GB10^3	GB (blue)	75.7	916 570	5260
	TB (red)	23.3	275 530	1581
ASE-GB10^3	GB	17.6	293 830	1686
	TB	82.4	1370 000	7863
ASE-GB10^2	GB	2.3	18 240	105
	TB	97.7	844 090	4844
ASE-GB10^1	GB	0.4	3970	23
	TB	99.6	1050 000	6026
ASE-GB_0	GB	0.00	0	0
	TB	100	760 760	4366

crystallographic information of the samples in Figure 3 about the misorientation angle between two neighboring lattices along the in-plane orientation, the ratio of GBs and TBs, the numbers of boundaries observed in an area of 174.24 μm^2, numbers per μm^2, and the boundary lengths.

2.4. Hole Carriers in ASE-Grown Cu(111) Films

To investigate the role of GBs in the NHE, we examined the transport properties of 2D Cu as a function of GB density. For this purpose, we chose 40 nm thick Cu films in which the NHE was most clearly observed (Figure 2f). The NHE of Cu films could be explained by the two-carrier model, and the estimated carrier densities of the Cu films with different thicknesses are shown in **Figure** 4a. The thickness dependence of the nonlinear Hall resistivity at $T = 2$ K is given in Figure S9a (Supporting Information). The samples with thicknesses of ≈40 nm show the maximum density of hole carriers and thicker samples than 200 nm approach to the 3D regime. The NHE of ultrathin samples less than 10 nm thick appears weak due to the incomplete growth of thin films.[30,31] Thus, samples in the intermediate thickness range ($d \approx 40$ nm) are the best option to investigate the transport properties of Cu in the 2D limit.

Figure 4b shows the magnetic field dependence of Hall effects measured in 2D Cu with different GB densities. As the GB density decreases, the NHE becomes clearer, and maximized when GB density decreases to zero, indicating that the hole carriers become dominating as the GB density decreases. In the GB-free sample, the scattering by GBs is minimized, so the scattering time of carrier becomes longer. The Hall effect, therefore, is strongly determined by the topology of the Fermi surface. The thickness dependence of the resistivity at $T = 2$ K follows the Fuchs–Sondheimer model, as shown in Figure S9b (Supporting Information), which confirms that the prepared samples have no GBs, as presented in the EBSD results in Figure 3e, and that TBs in SCCFs are not scatterers of electrons during transport.[32,33] The estimated carrier density and mobility of 2D Cu with different GB densities are summarized in Figure 4c,d. The nonlinearity of the Hall resistivity increases with decreasing temperature (Figure S10a, Supporting Information), and thus, the hole density also abruptly increases to 5.2 × 10^{22} cm^{-3} (Figure 4c; Figure S10b, Supporting Information) when the GBs are completely suppressed to zero density, 0 μm^{-2}. In contrast, the electron density decreases as the GB density decreases (Figure 4c). This observation indicates that the carriers located on the outermost Fermi surface (Figure 1b), characterized by the highest v_F, exhibit hole-like behavior. Indeed, the roughly consistent hole carrier density of 3.8 × 10^{22} cm^{-3} could be estimated from the ARPES measurement, through the occupied volume of the hole Fermi surface within the Brillouin zone (BZ; Figure S1, Supporting Information). Conversely, the presence of surface or grain boundaries leads to an increase in carriers occupying the inner Fermi surfaces. This is due to the increase of potential energy when the carriers collide with the surface or GBs, resulting in a decrease in kinetic energy and Fermi velocity. As a result, carriers that scatter frequently from surfaces or GBs will direct their paths to the inner circle and ultimately occupy electron orbitals.

The ratio of hole density to electron density is presented in the inset of Figure 4c, where the HCD transport becomes more remarkable as the GB density approaches zero. Notably, the mobility of electrons in 2D single-crystal Cu without GBs reaches ≈400 cm^2 V^{-1} s^{-1} (Figure 4d; Figure S10b, Supporting Information), while the mobility of electrons in bulk Cu remains only ≈20–60 cm^2 V^{-1} s^{-1}.[34]

As the thickness of the thin film decreases, the density of TB increases near the interface area with the substrate. While TBs do not seriously affect electron motion, balancing the minimum thickness and minimum twin boundaries allows us to achieve the highest hole carrier density, which in this study is observed at 40 nm. Although the 80 nm thick film is twice as thick as the 40 nm film, we believe that the reason why the NHE is not significantly reduced is that more TB-reduced regions appear at the top, which intensifies hole-like behavior. These properties are maintained in films up to 200 nm thick when the films are free of GB.

3. Conclusion

The electronic structure observed by ARPES and the abnormal nonlinearity in 2D single crystals with zero GB density reveal the role of GBs in the electron flow in Cu; even a low density of GBs can hide the critical nature of transport in the noble metal. Another important scientific finding with GB engineering is that TBs can be almost invisible to the electrons in 2D Cu. The elongated MFP and coherency of charge carriers in the absence of GBs generate HCD transport, reflecting the increase in carriers occupying the outermost concave Fermi surface with the largest v_F in 2D Cu. We suggest that the transport by hole carriers in 2D copper is the intrinsic characteristic of 2D Cu that has been screened by the scattering of electrons at GBs.

4. Experimental Section

Preparation of Single-Crystal Cu Thin Films via the ASE Technique: Cu thin films were fabricated with high-quality crystallinity as GB-free single crystals and GB density-controlled single crystals using the ASE technique.[13] The ASE system was a modified Radio-frequency (RF) sputtering system improved by employing a single-crystal sputtering target, replacing conventional electric conductors with single-crystal conductors and employing a mechanical noise reduction (MNR) system. The optimum growth temperature was ≈170 °C and varied by ±10 °C depending on the system. Al_2O_3 was utilized as a substrate for growing SCCF samples.

© 2024 The Author(s). Advanced Materials published by Wiley-VCH GmbH

15214095, 2024, 36, Downloaded from https://onlinelibrary.wiley.com/doi/10.1002/adma.202403783, Wiley Online Library on [12/09/2024]. See the Terms and Conditions (https://onlinelibrary.wiley.com/terms-and-conditions) on Wiley Online Library for rules of use; OA articles are governed by the applicable Creative Commons License

15214095, 2024, 36, Downloaded from https://onlinelibrary.wiley.com/doi/10.1002/adma.202403783, Wiley Online Library on [12/09/2024]. See the Terms and Conditions (https://onlinelibrary.wiley.com/terms-and-conditions) on Wiley Online Library for rules of use; OA articles are governed by the applicable Creative Commons License

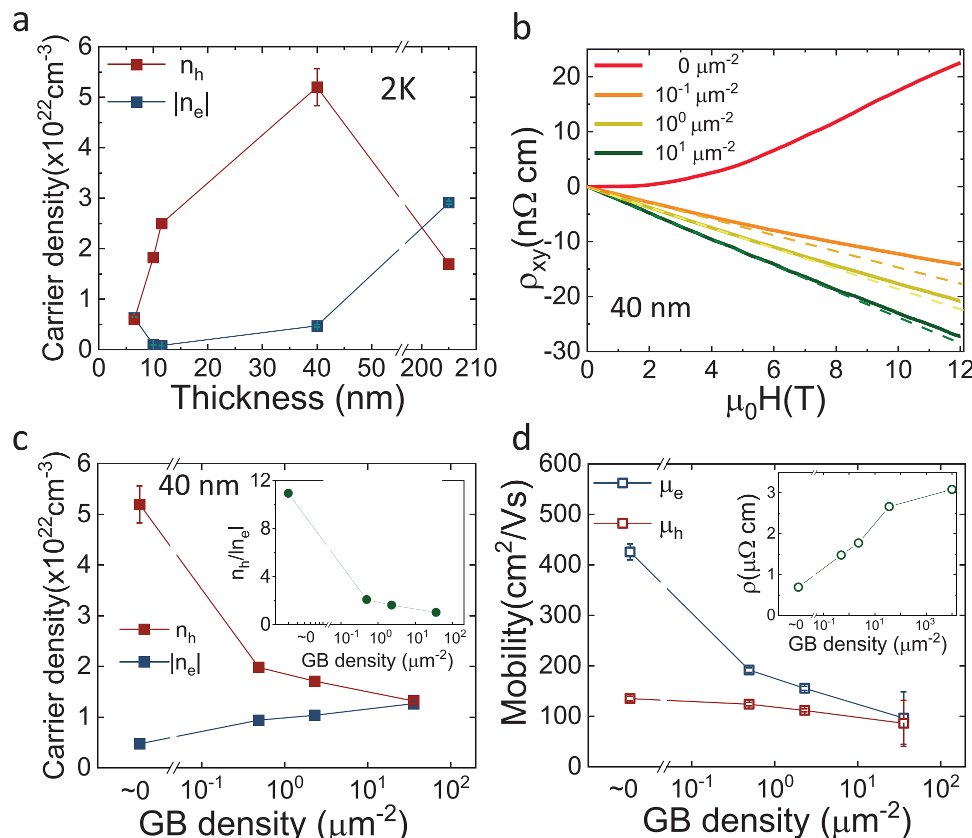

Figure 4. Carrier density, resistivity, and mobility as a function of the thickness and density of GBs. a) Carrier density at $T = 2$ K as a function of thickness. The carrier density is determined by the two-carrier model based on the Hall resistivity. b) Hall resistivity and c) carrier density of 40 nm Cu films with different GB densities at $T = 2$ K. The dashed lines in panel (b) are straight lines to clearly show the nonlinearity. d) Mobility at $T = 2$ K as a function of GB density. The insets of panels (c) and (d) show the ratio of hole density to electron density and the resistivity at $T = 2$ K, respectively. The error bars represent the 95% confidence limit.

The Al_2O_3 substrate was a 2 in. wafer with a thickness of 0.43 mm, featuring a surface roughness of 0.25 nm RMS roughness. The in-plane atomic distance mismatch between Cu atoms in the film and O atoms in Al_2O_3, calculated as $f((d^{[\bar{1}20]}_{O-O\ Al_2O_3} - d^{[\bar{1}10]}_{Cu-Cu})/d^{[\bar{1}20]}_{O-O\ Al_2O_3})$, is estimated to be 6.9%. However, considering the extended atomic distance mismatch (EADM),[35,36] significant mechanical misfit strain can be relieved if the mismatch for a relatively long period of atomic distance is extremely small. EADM is defined as $(ID - I'D')/I'D'$, where D and D' are the Cu–Cu distance in the Cu (111) epilayer and the O–O distance in the substrate, respectively, and I and I' are the smallest nonreducible integers determined by the relation $D{:}D' \sim I{:}I'$. Given the interatomic spacing of Cu atoms in the film $D_{Cu\text{-}Cu}$ ($14 \times d^{[\bar{1}10]}_{Cu-Cu}$) = 3.578 nm) and the interatomic spacing of O atoms in Al_2O_3 (D'_{O-O} ($13 \times d^{[\bar{1}20]}_{O-O\ Al_2O_3}$)= 3.575 nm), the EADM of the Cu–Al_2O_3 interface is ≈0.1%. For control of the GB density, the pristine 40 nm thick sample was intentionally grown at 100 °C to obtain a certain number of GBs and adjusted the number of GBs by additional thermal treatments. The numbers of GBs and TBs were obtained very precisely by EBSD mapping with the misorientation line distribution in RD mode (see the "Structural Characterizations" section). Ar gas (99.9999%, 6 N) was used for the deposition atmosphere. The relationship between the deposition time and the thickness of the thin film (or the average growth rate) was determined from the average deposition time of a 200 nm thick film grown under the optimum conditions. The determined average growth rate of ≈4.3 nm min^{-1} is fairly reliable above a film thickness of 10 nm. The initial pressure in the RF sputtering was below 2×10^{-7} Torr, and the working pressure was controlled by injecting argon gas (99.9999%) to 5.4 $\times 10^{-3}$ Torr. The RF power and the rotation rate were 25 W and 30 RPM, respectively. The thickness of the film was controlled by the deposition time and confirmed with atomic force microscopy (AFM). The ultraflat surface of SCCF, with an RMS roughness of ≈0.15 nm, is displayed in Figure S11 (Supporting Information). The atomic structures of cross-sectional copper films were observed on annular dark field (ADF) imaging mode by aberration-corrected scanning transmission electron microscope (STEM, JEM-ARM200CF, JEOL) operating at 200 kV with a probe-forming angle of ≈23 mrad. The angle range of ADF detector was set to be 45–170 mrad.

Growing Grain Boundary-Free Thin Films: There are two ways to grow grain boundary-free single crystal thin films.

1) *Growth of Samples without GBs from the Beginning*: When thin films are grown using the ASE method with well-optimized growth conditions, they grow without GBs from the pristine samples.[9] The crystal growth process by the ASE method goes through three stages: 1) nucleation and lateral growth, 2) coherent merging, and 3) layer growth to a single-crystal film. The ASE method involves accurately sputtering atoms one by one from a single crystal target and supplying them to the substrate successively. Thus, through this process, no clusters can be stacked, no grain boundaries are formed, and the entire film is completely aligned to the (111) plane. Nevertheless, TBs exist even in the single-crystal thin film, and the formation mechanism of TBs is different from that of GBs. It was confirmed that, in transport measurements, the TB dependence was negligible, whereas the dependence on GBs was very critical, so it was focused on growing a single-crystal thin film without GBs. The nonlinear Hall effects obtained in Figure 2d–h

© 2024 The Author(s). Advanced Materials published by Wiley-VCH GmbH

were all from samples grown without GBs from the beginning (without post heat treatment).

2) *Elimination of GBs by Post Heat Treatment*: The sample used for Figure 3b was intentionally produced to have GBs by using a condition (100 °C) other than the optimized condition (180 °C) to investigate GB dependence. The pristine sample grown at about 100 °C, which was not optimal, had a GB density of about 10^1 μm^{-2}, while the commercial sample (Figure 3a) had a GB density of 10^3–10^5 μm^{-2}. GB density can be adjusted by vacuum heat treatment. However, it is not simple to reduce GBs by heat treatment because the degree of GB reduction does not have a strictly linear relationship with temperature and depends on several variables such as the thicknesses of Cu thin films. Samples in Figure 3c–e were heat-treated at 450, 500, and 400 °C for ≈30 min, respectively. Among them, the sample heat-treated at 400 °C was found to be grain boundary free. The heat treatment chamber was filled with an inert gas, and heat treatment was performed for 30 min in an oxygen-free atmosphere.

Structural Characterizations: EBSD images were obtained using a SUPRA40 VP system (Carl Zeiss AG, Oberkochen, Germany), which was equipped with a fully automated device attachment including an EDAX-TSL Hikari EBSD detector. EBSD maps were acquired using a spatial step size of 80 nm on a hexagonal grid. The area size of a single mapping was ≈174.3 μm^2. The average confidence index of the Kikuchi maps during the EBSD scans generally varied between 0.80 and 0.90. However, for the polycrystal Cu film, the index was at a level of 0.7. The misorientation statistics were derived from the EBSD maps with TSL OIM analysis v7 (Ametek, Inc). A segment between two neighboring points was considered a boundary if the misorientation was larger than 1°. On the misorientation maps, the boundaries with a misorientation angle between 0.0° and 59.0° were indicated by blue lines, which correspond to GBs, and the boundaries with a misorientation angle between 59.0° and 60.0° were indicated by red lines, which are associated with the TBs of face-centered cubic (FCC) (111) structures. The crystallinity of the grown samples was also examined by X-ray diffraction (XRD) and grazing-incidence XRD (GIXRD) as displayed in Figure S12 (Supporting Information). Compared to the PCCF, SCCF shows high crystallinity without any nanostructure.

ARPES Measurement: High-resolution ARPES measurements were conducted at beamline 4.0.3 of the Advanced Light Source (ALS). Cu thin films were annealed under ultrahigh vacuum with a pressure better than 5×10^{-10} Torr and measured at 10 K, with pressure better than 5×10^{-11} Torr. Data in the main text were collected using incident light with a photon energy of 120 eV, which corresponds to the $k_z = 0$ (Γ) in the 3D Brillouin zone, and both linear horizontally and vertically polarized light were used to exclude unwanted matrix element effects. Photon energy-dependent ARPES was conducted by using linear horizontally polarized light with photon energies from 40 to 120 eV (Figure S3, Supporting information). The overall energy and angle resolutions were set to be better than 20 meV and 0.1°.

Hall Measurement and Sample Preparation: A Hall-bar device of Cu thin films on sapphire substrates was fabricated by e-beam lithography and wet etching with $FeCl_3$ solution. The typical device channel length and width were 200 and 20 μm, respectively. Electrical transport measurements of the Cu thin film devices were conducted by a TeslatronPT (Oxford) over a temperature range from $T = 1.5$ to 300 K. A magnetic field (up to 12 T) was applied along the direction vertical to the planar surface of the Cu thin films. A DC current was applied to the device by a Keithley 4200 or 6221 current generator, and the longitudinal (for resistivity and magnetoresistance) and transverse (for Hall) voltage differences were simultaneously measured by multiple Keithley 2182A voltmeters. The applied current was on the order of mA.

Two-Carrier Model Fitting: For the NHE, the carrier density and mobility were derived from fitting of the Hall resistivity with the two-carrier model. The Hall resistivity with two carriers is given as

$$\rho_{xy} = \frac{t}{e} B \frac{\left(\mu_e^2 n_e + \mu_h^2 n_h\right) + \mu_e^2 \mu_h^2 (n_e + n_h) B^2}{\left(\mu_e |n_e| + \mu_h |n_h|\right)^2 + \mu_e^2 \mu_h^2 (n_e + n_h)^2 B^2} \quad (1)$$

where t is the thickness of the film, B is the applied magnetic field, e is the electronic charge, and n_e (n_h) and μ_e (μ_h) are the carrier density and mobility of electrons (holes).[37] n_e (n_h) and μ_e (μ_h) are the fitting parameters. The Hall resistivity $\rho_{xy}(B)$ was fitted with the constraint of the longitudinal resistivity at zero magnetic field, ρ_{xx} $(B = 0) = \frac{t}{e} \frac{1}{(\mu_e |n_e| + \mu_h |n_h|)}$. The error bars of the carrier density and mobility of electrons (holes) were calculated within the 95% confidence limit with fixed carrier density and mobility of electrons (holes) at optimized values.

Theoretical Calculations: All ab initio electronic structure calculations were performed with density functional theory (DFT) using the generalized gradient approximation (GGA) Perdew–Burke–Ernzerhof functional[38] and with the projected augmented plane-wave method,[39] as implemented by Kresse et al.[40] The Cu thin film was represented by a slab of 42 layers with the theoretical equilibrium lattice constant. A vacuum length of 20 Å was used, and the middle two layers of the slab were fixed in their bulk positions. The electron wavefunctions were expanded in a plane-wave basis set with a cut-off energy of 400 eV. The Brillouin zone for the slabs was sampled using a (5 × 5 × 1) Monkhorst–Pack k-point grid.[41] Fermi surfaces were generated by using IFermi software by Ganose et al.[42]

Supporting Information

Supporting Information is available from the Wiley Online Library or from the author.

Acknowledgements

J.M.O., K.K., and J.H. contributed equally to this work. This research was supported by the Basic Science Research Program through the National Research Foundation of Korea (NRF) funded by the Ministry of Science, ICT & Future Planning (Grant Nos. RS-2024-00340377, NRF-2021R1A2C1013119, and NRF-2021R1A5A1032937), a Korea Basic Science Institute (National Research Facilities and Equipment Center) grant funded by the Ministry of Education (Grant No. 2021R1A6C101A429), a National Research Foundation of Korea (NRF) grant funded by the Korean government (MSIT) (RS-2023-00210295), BrainLink program funded by the Ministry of Science and ICT through the National Research Foundation of Korea (Grant No. 2022H1D3A3A01077468), National Measurement Standard Services and Technical Services for SME funded by Korea research Institute of Standards and Science (Grant No. KRISS-2022-GP2022-0014), and the Samsung Science and Technology Foundation under Project Number SRFC-MA2202-02. Use of the ALS, Lawrence Berkeley National Laboratory, is supported by the U.S. Department of Energy, Office of Science, Office of Basic Energy Sciences under Contracts No. DE-AC02-05CH11231.

Conflict of Interest

The authors declare no conflict of interest.

Data Availability Statement

The data that support the findings of this study are available in the supplementary material of this article.

Keywords

grain boundary free, hole carriers in Cu, nonlinear Hall effect, single-crystal copper thin film, triangular hole orbit

Received: March 14, 2024
Revised: June 24, 2024
Published online: July 18, 2024

© 2024 The Author(s). Advanced Materials published by Wiley-VCH GmbH

15214095, 2024, 36, Downloaded from https://onlinelibrary.wiley.com/doi/10.1002/adma.202403783, Wiley Online Library on [12/09/2024]. See the Terms and Conditions (https://onlinelibrary.wiley.com/terms-and-conditions) on Wiley Online Library for rules of use; OA articles are governed by the applicable Creative Commons License

[1] Y. C. Cho, M. Ajmal, W.-K. Kim, C. R. Cho, S.-Y. Jeong, J. H. Park, S. E. Park, S. Park, H.-K. Pak, H. C. Kim, *Cryst. Growth Des.* **2010**, *10*, 2780.
[2] W. Steinhögl, G. Steinlesberger, M. Traving, M. Engelhardt, *J. Appl. Phys.* **2005**, *97*, 023706.
[3] L. VJ, N. P. Kobayashi, M. S. Islam, W. Wu, P. Chaturvedi, N. X. Fang, S. Y. Wang, R. S. Williams, *Nano Lett.* **2009**, *9*, 178.
[4] N. Formica, D. S. Ghosh, A. Carrilero, T. L. Chen, R. E. Simpson, V. Pruneri, *ACS Appl. Mater. Interfaces* **2013**, *5*, 3048.
[5] R. A. Maniyara, D. Rodrigo, R. Yu, J. Canet-Ferrer, D. S. Ghosh, R. Yongsunthon, D. E. Baker, A. Rezikyan, F. J. G. de Abajo, V. Pruneri, *Nat. Photonics* **2019**, *13*, 328.
[6] A. Jamnig, N. Pliatsikas, G. Abadias, K. Sarakinos, *Appl. Surf. Sci.* **2021**, *538*, 148056.
[7] S. Dutta, K. Sankaran, K. Moors, G. Pourtois, S. Van Elshocht, J. Bömmels, W. Vandervorst, Z. Tökei, C. Adelmann, *J. Appl. Phys.* **2017**, *122*, 025107.
[8] A. Jog, T. Zhou, D. Gall, *IEEE Trans. Electron Devices* **2021**, *68*, 257.
[9] T. Ha, Y.-S. Seo, T.-T. Kim, B. Lamichhane, Y.-H. Kim, S. J. Kim, Y. Lee, J. C. Kim, S. E. Park, K. I. Sim, J. H. Kim, Y. I. Kim, S. J. Kim, H. Y. Jeong, Y. H. Lee, S.-G. Kim, Y.-M. Kim, J. Hwang, S.-Y. Jeong, *Nat. Commun.* **2023**, *14*, 685.
[10] P. J. W. Moll, P. Kushwaha, N. Nandi, B. Schmidt, A. P. Mackenzie, *Science* **2016**, *351*, 1061.
[11] S.-Y. Yang, Y. Wang, B. R. Ortiz, D. Liu, J. Gayles, E. Derunova, R. Gonzalez-Hernandez, L. Šmejkal, Y. Chen, S. S. P. Parkin, S. D. Wilson, E. S. Toberer, T. McQueen, M. N. Ali, *Sci. Adv.* **2020**, *6*, eabb6003.
[12] S. J. Kim, Y. I. Kim, B. Lamichhane, Y.-H. Kim, Y. Lee, C. R. Cho, M. Cheon, J. C. Kim, H. Y. Jeong, T. Ha, J. Kim, Y. H. Lee, S.-G. Kim, Y.-M. Kim, S.-Y. Jeong, *Nature* **2022**, *603*, 434.
[13] S. J. Kim, S. Kim, J. Lee, Y. Jo, Y.-S. Seo, M. Lee, Y. Lee, C. R. Cho, J.-P. Kim, M. Cheon, J. Hwang, Y. I. Kim, Y.-H. Kim, Y.-M. Kim, A. Soon, M. Choi, W. S. Choi, S.-Y. Jeong, Y. H. Lee, *Adv. Mater.* **2021**, *33*, 2007345.
[14] M. Sagmeister, U. Brossmann, S. Landgraf, R. Würschum, *Phys. Rev. Lett.* **2006**, *96*, 156601.
[15] D. Daghero, F. Paolucci, A. Sola, M. Tortello, G. A. Ummarino, M. Agosto, R. S. Gonnelli, J. R. Nair, C. Gerbaldi, *Phys. Rev. Lett.* **2012**, *108*, 066807.
[16] H. Nakayama, J. Ye, T. Ohtani, Y. Fujikawa, K. Ando, Y. Iwasa, E. Saitoh, *Appl. Phys. Express* **2012**, *5*, 023002.
[17] T. A. Petach, M. Lee, R. C. Davis, A. Mehta, D. Goldhaber-Gordon, *Phys. Rev. B* **2014**, *90*, 081108.
[18] N. P. Ong, *Phys. Rev. B: Condens. Matter Mater. Phys.* **1991**, *43*, 193.
[19] A. Carrington, A. P. Mackenzie, C. T. Lin, J. R. Cooper, *Phys. Rev. Lett.* **1992**, *69*, 2855.
[20] H. Y. Hwang, B. Batlogg, H. Takagi, H. L. Kao, J. Kwo, R. J. Cava, J. J. Krajewski, W. F. Peck Jr., *Phys. Rev. Lett.* **1994**, *72*, 2636.
[21] N. E. Hussey, *Phys. Rev. B: Condens. Matter Mater. Phys.* **2008**, *20*, 123201.
[22] A. I. Coldea, M. D. Watson, *Annu. Rev. Condens. Matter Phys.* **2018**, *9*, 125.
[23] M. J. Eom, S. W. Na, C. Hoch, R. K. Kremer, J. S. Kim, *Phys. Rev. B* **2012**, *85*, 024536.
[24] S. Zhang, Q. Wu, Y. Liu, O. V. Yazyev, *Phys. Rev. B* **2019**, *99*, 035142.
[25] F. Baumberger, W. Auwärter, T. Greber, J. Osterwalder, *Science* **2004**, *306*, 2221.
[26] C. Kittel, *Introduction to Solid State Physics*, John Wiley & Sons, Hoboken, NJ, **1986**.
[27] N. Nagaosa, J. Sinova, S. Onoda, A. H. MacDonald, N. P. Ong, *Rev. Mod. Phys.* **2010**, *82*, 1539.
[28] S. Lee, H.-Y. Park, S. J. Kim, H. Lee, I.-J. Lee, C. R. Cho, E. Lee, S.-Y. Jeong, Y. H. Lee, *ACS Appl. Nano Mater* **2019**, *2*, 3300.
[29] L. Lu, Y. Shen, X. Chen, L. Qian, K. Lu, *Science* **2004**, *304*, 422.
[30] S. K. So, H. H. Fong, C. F. Yeung, N. H. Cheung, *Appl. Phys. Lett.* **2000**, *77*, 1099.
[31] K.-H. Müller, M. M. A. Yajadda, *J. Appl. Phys.* **2012**, *111*, 123705.
[32] E. H. Sondheimer, *Adv. Phys.* **1952**, *1*, 1.
[33] G. Kästle, H.-G. Boyen, A. Schröder, A. Plettl, P. Ziemann, *Phys. Rev. B* **2004**, *70*, 165414.
[34] V. Palenskis, *World J. Condens. Matter Phys.* **2013**, *03*, 73.
[35] T. Kato, P. Kung, A. Saxler, C.-J. Sun, H. Ohsato, M. Razeghi, T. Okuda, *J. Cryst. Growth* **1998**, *183*, 131.
[36] X.-Y. Liu, L. Arslan, B. W. Arey, J. Hackley, V. Lordi, C. J. K. Richardson, *ACS Nano* **2018**, *12*, 6843.
[37] J. S. Kim, S. S. A. Seo, M. F. Chisholm, R. K. Kremer, H.-U. Habermeier, B. Keimer, H. N. Lee, *Phys. Rev. B* **2010**, *82*, 201407.
[38] G. Kresse, J. Furthmuller, *Phys. Rev. B* **1996**, *54*, 11169.
[39] P. E. Blöchl, *Phys. Rev. B: Condens. Matter Mater. Phys.* **1994**, *50*, 17953.
[40] J. P. Perdew, K. Burke, M. Ernzerhof, *Phys. Rev. Lett.* **1996**, *77*, 3865.
[41] H. J. Monkhorst, J. D. Pack, *Phys. Rev. B* **1976**, *13*, 5188.
[42] A. M. Ganose, A. Searle, A. Jain, S. M. Griffin, *J. Open Source Software* **2021**, *6*, 3089.

© 2024 The Author(s). Advanced Materials published by Wiley-VCH GmbH

15214095, 2024, 36, Downloaded from https://onlinelibrary.wiley.com/doi/10.1002/adma.202403783, Wiley Online Library on [12/09/2024]. See the Terms and Conditions (https://onlinelibrary.wiley.com/terms-and-conditions) on Wiley Online Library for rules of use; OA articles are governed by the applicable Creative Commons License